ELSEVIER

International Journal of Thermal Sciences 41 (2002) 721–736

International Journal of Thermal Sciences

www.elsevier.com/locate/ijts

Compressible heat transfer computations by an adaptive finite element method

É. Turgeon [a], D. Pelletier [a,*], F. Ilinca [b]

[a] *Département de Génie Mécanique, École Polytechnique de Montréal, Montréal, PQ, Canada, H3C 3A7*
[b] *Industrial Materials Institute National Research Council of Canada 75, de Mortagne, Boucherville, PQ, Canada, J4B 6Y4*

Received 18 June 2001; accepted 11 September 2001

Abstract

This paper presents adaptive finite element computations of laminar jet impingement heat transfer. Variable fluid properties and compressibility effects are considered. A unified formulation of the equations is used to treat the simultaneous presence of three flow regimes: incompressible ($\rho = constant$), compressible ($\rho = \rho(p, T)$), and anelastic ($\rho = \rho(T)$). The error estimator uses a local least squares projection method and accounts for errors in velocity, pressure and temperature. The performance of the methodology is verified by solving a problem possessing a closed form solution. Several applications are then considered. We study two different gases (air and CO_2), different conditions (heated, cooled or constant properties), compressibility and inlet velocity profile effects. Heat transfer is a key element of the study. Results indicate that the methodology can produce grid independent solutions even for derived quantities and in thin boundary layers.

1. Introduction

Impinging round jets are encountered in many industrial applications such as cooling of turbine blades and electronic components, drying of textile or paper, annealing of metal and plastic sheets, and tempering of glass. The very high heat transfer coefficients they generate make them particularly attractive for such operations. This has motivated much research on this topic. Reviews of the literature for impinging jets are provided by Martin [1], Downs and James [2], Polat et al. [3], and Jambunathan et al. [4]. Both experimental and numerical studies were performed.

Numerical methods have become an important tool for the study of such heat transfer problems. They make it possible to understand, analyze, and optimize the performance of a given system at lower costs than with experimental studies. The diversity of behaviors exhibited by impinging jets makes them interesting from a numerical point of view. These flows contain thin boundary and shear layers, impingement regions, free and wall jets, stagnation points, streamline curvature, heat transfer etc. .... Such diversity constitutes a demanding test for numerical simulation codes.

Accuracy is a key element in computational heat transfer. Yet, authors often report results from a single mesh computation without performing any grid refinement studies. Hence, the accuracy of their predictions cannot be assessed. Adaptive methods provide a powerful approach to control and maximize the accuracy of the numerical solution. The error estimator quantifies the error and the adaptivity becomes a simple means of automating systematic grid refinement studies. The objective of the present paper is to show that adaptive remeshing can yield numerically exact (i.e., grid independent) solutions of the differential equations of convective heat transfer. This control of the discretization error ensures that differences between numerical predictions and measurements are due to mathematical modeling decisions. Analysis and assessments of the results may then be performed rigorously and on a solid basis.

The adaptive methodology used in the present paper has been previously used with success by the authors. It was applied to the solution of turbulent flows [5–7], heat transfer [8–10], compressible flows [11–13], impinging jets [14,15], and heat transfer with variable fluid properties [16]. In this paper, we restrict our study to laminar flows. Difficulties arise from the fact that all physical properties of the fluid are variable. In particular, density variations may be due to either pressure or temperature. This provides significant

* Correspondence and reprints.
E-mail address: dominique.pelletier@polymtl.ca (D. Pelletier).

1290-0729/02/$ – see front matter
PII: S1290-0729(02)01367-4

Nomenclature

C_f	local skin friction coefficient
c_p	specific heat at constant pressure
d	pipe diameter
Ec	Eckert number
$\boldsymbol{f}$	body force
M	Mach number
Nu	Nusselt number
p	pressure
Pr	Prandtl number
q_s	heat source
q_w	wall heat flux
R	Thermodynamic constant of gas
Re	Reynolds number
T	temperature
$\boldsymbol{u}$	velocity
u, v	velocity components
U_r	reference velocity
x, r	cylindrical coordinates
γ	ratio of specific heats
λ	thermal conductivity
μ	viscosity
ρ	density
τ_w	wall shear stress

Subscripts

r	reference value
s	scale
tot	total quantity
w	at the wall
∞	at infinity (ambient condition)

Superscripts

$\sim$	dimensionless value

challenges for a numerical study. The aim is to assess the effects of pressure and temperature on density and their impact on the heat transfer characteristic of the impinging jet. The effect of temperature dependent fluid properties will also be assessed. The task is thus to develop a simulation tool capable of dealing with the following flow regimes:

- Incompressible flow, $\rho = constant$,
- Anelastic flow, $\rho = \rho(T)$,
- Compressible flow, $\rho = \rho(p, T)$.

It must also account for constant or temperature dependent fluid properties. It is important that the numerical method be able to deal with the above flow regimes for at least two reasons. First, the three regimes may be simultaneously present in various parts of the flow domain. Second, assessments of various effects is significantly simplified if the same numerical method is used for comparing two different flow regimes, say, incompressible and compressible flows.

For the comparison study, two objectives were set. The first one is to study highly heated or cooled impinging gas jets for which fluid properties are temperature dependent. These anelastic flows are compared with constant property solutions to highlight the effects of variable fluid properties. Much work on impinging jets may be found in the literature, but few have considered variable fluid properties. Aihara et al. [17] performed such a study, but did not rigorously assess the accuracy of their predictions. Here the emphasis is on achieving high accuracy through adaptivity (i.e., obtaining grid independent solutions). The second objective is to assess the effect of compressibility of impinging jets at high subsonic *Mach* numbers. This constitutes a first step towards the more general and interesting case of turbulent compressible impinging jets. Typical applications involve hovercraft or other ground-effects machines and vertical/short takeoff and landing (V/STOL) configurations.

The paper is organized as follows. First, the governing equations, their dimensionless form, and the details of a formulation applicable to all flow regimes are presented. The numerical solution procedure, the error estimator, and the adaptive methodology are then briefly described. This is followed by a grid refinement study for a problem possessing a closed form solution. This verifies the performance of the adaptive procedure. The methodology is then applied to a variety of impinging jets. The paper ends with the conclusions.

2. Modeling of the problem

2.1. Governing equations

The flow regime of interest is steady, laminar, compressible, with variable fluid properties, and includes heat transfer effects. It is modeled by the continuity, Navier–Stokes, and energy equations:

$$\begin{aligned} &-\nabla\cdot\boldsymbol{u} = \frac{1}{\rho}\boldsymbol{u}\cdot\nabla\rho \\ &\rho\boldsymbol{u}\cdot\nabla\boldsymbol{u} \\ &\quad = -\nabla p + \nabla\cdot\left[\mu\left(\nabla\boldsymbol{u} + \nabla\boldsymbol{u}^{\mathrm{T}}\right) - \frac{2}{3}\mu\boldsymbol{I}\nabla\cdot\boldsymbol{u}\right] + \rho\boldsymbol{f} \\ &\rho c_p\boldsymbol{u}\cdot\nabla T = \boldsymbol{u}\cdot\nabla p + \nabla\cdot(\lambda\nabla T) + \rho q_s \end{aligned} \tag{1}$$

where $\boldsymbol{u}$ is the velocity, ρ the density, p the pressure, μ the fluid viscosity, $\boldsymbol{I}$ the identity matrix, $\boldsymbol{f}$ a body force, c_p the specific heat at constant pressure, T the temperature, λ the thermal conductivity, and q_s a heat source. The fluid

Table 1
Temperature dependent gas properties

	air	CO_2
c_p/c_{p_r}	$(T/T_r)^{0.05}$	$(T/T_r)^{0.34}$
μ/μ_r	$(T/T_r)^{0.68}$	$(T/T_r)^{1.5}\dfrac{1+230/T_r}{T/T_r+230/T_r}$
λ/λ_r	$(T/T_r)^{0.76}$	$(T/T_r)^{1.5}\dfrac{1+(1440/T_r)^2}{(T/T_r)^2+(1440/T_r)^2}$

properties μ, c_p, and λ are either constant or temperature-dependent. The temperature dependence used here is given in Table 1. These relationships correspond to the correlations suggested by Aihara et al. [17], which are valid between 280 K and 650 K. Finally, the subscript r denotes a reference state.

For compressible flows, an equation of state is required to relate density to pressure and temperature. In the present paper we consider the equation of state for a perfect gas:

$$\rho = \frac{p}{RT} \tag{2}$$

In this expression R is the thermodynamic constant of the gas. Dirichlet and Neumann boundary conditions complete the statement of the problem.

A pressure based finite element method is used to solve the above equations. Hence only velocity, pressure, and temperature are discretized. When density is required, it is evaluated through the equation of state. Thus, the right-hand side of the continuity equation can be expressed in terms of pressure and temperature:

$$-\nabla\cdot\boldsymbol{u} = \frac{1}{p}\boldsymbol{u}\cdot\nabla p - \frac{1}{T}\boldsymbol{u}\cdot\nabla T \tag{3}$$

Although mathematically correct, this dimensional form of the equations may lead to numerical difficulties. The resulting system of algebraic equations may be ill-conditioned or the formulation may contain indeterminacies for certain limiting flow cases. For example, taking the limit of vanishing Mach number or incompressibility of the above equations may not explicitly yield the usual equations for strongly heated or incompressible flow. Indeterminacies may still have to be lifted to achieve a well posed final result. A nondimensional form of the equations can shed light on this issue and can also ease interpretation of results.

2.2. Dimensionless equations

There exist several ways to nondimensionalize the equations. Usually, a particular choice is suited to a limited range of problems. In the present paper, incompressible flows ($\rho = constant$), truly compressible flows ($\rho = \rho(p,T)$), and anelastic flows ($\rho = \rho(T)$) are considered. Thus, it is desirable to have one simulation code, based on a unified formulation, capable of treating all these flow regimes. This formulation must be free of singularities or indeterminacies for the limit cases. This is important for two reasons. First, there exist flows for which several of the previously mentioned flow regimes may be present simultaneously in different regions of the domain. Second, a single simulation code using a unified formulation increases the likelyhood that observed differences between simulations are due to differences in the mathematical models of the flow physics rather than to differences in the numerics used for each model.

A common dimensionless form in external compressible aerodynamics is obtained by a simple scaling:

$$\tilde{x} = \frac{x}{L_r}, \qquad \tilde{T} = \frac{T}{T_r}, \qquad \tilde{\rho} = \frac{\rho}{\rho_r}, \qquad \tilde{\mu} = \frac{\mu}{\mu_r}$$
$$\tilde{\boldsymbol{u}} = \frac{\boldsymbol{u}}{U_r}, \qquad \tilde{p} = \frac{p}{p_s}, \qquad \tilde{c}_p = \frac{c_p}{c_{p_r}}, \qquad \tilde{\lambda} = \frac{\lambda}{\lambda_r}$$

where $p_s = \rho_r U_r^2$ is a pressure scale. The subscript r stands for a reference state, typically the free stream conditions. Note that a single location for defining the reference thermodynamic state ensures that it satisfies the equation of state:

$$p_r = \rho_r R T_r$$

Introduction of a reference Mach number

$$M_r = \frac{U_r}{\sqrt{\gamma_r R T_r}}$$

of the thermodynamic equality

$$c_{p_r} = \frac{\gamma_r R}{\gamma_r - 1}$$

and some manipulations leads to the following dimensionless system:

$$\begin{aligned}
&-\widetilde{\nabla}\cdot\tilde{\boldsymbol{u}} = \frac{1}{\tilde{p}}\tilde{\boldsymbol{u}}\cdot\widetilde{\nabla}\tilde{p} - \frac{1}{\widetilde{T}}\tilde{\boldsymbol{u}}\cdot\widetilde{\nabla}\widetilde{T}\\
&\tilde{\rho}\tilde{\boldsymbol{u}}\cdot\widetilde{\nabla}\tilde{\boldsymbol{u}}\\
&\quad = -\widetilde{\nabla}\tilde{p} + \frac{1}{Re}\widetilde{\nabla}\cdot\left[\tilde{\mu}\left(\widetilde{\nabla}\tilde{\boldsymbol{u}} + \widetilde{\nabla}\tilde{\boldsymbol{u}}^{\mathrm{T}}\right) - \frac{2}{3}\tilde{\mu}\boldsymbol{I}\widetilde{\nabla}\cdot\tilde{\boldsymbol{u}}\right] + \tilde{\rho}\tilde{\boldsymbol{f}}\\
&\tilde{\rho}\tilde{c}_p\tilde{\boldsymbol{u}}\cdot\widetilde{\nabla}\widetilde{T}\\
&\quad = (\gamma_r - 1)M_r^2\tilde{\boldsymbol{u}}\cdot\widetilde{\nabla}\tilde{p} + \frac{1}{Re\,Pr}\widetilde{\nabla}\cdot\left(\tilde{\lambda}\widetilde{\nabla}\widetilde{T}\right) + \tilde{\rho}\tilde{q}_s\\
&\tilde{\rho} = \gamma_r M_r^2\frac{\tilde{p}}{\widetilde{T}}
\end{aligned} \tag{4}$$

where

$$Re = \frac{\rho_r U_r L_r}{\mu_r}, \qquad Pr = \frac{\mu_r c_{p_r}}{\lambda_r}$$

These equations are well suited for compressible flows but they experience problems in the limit of vanishing Mach number. One might mistakenly conclude from the equation of state that density goes to zero as the Mach number vanishes while, in fact, the appropriate conclusion is that pressure behaves as the inverse of the Mach number squared. This dimensionless form contains an indeterminacy in the limit of vanishing Mach number.

This problem is due to an improper nondimensionalization of pressure. In the present form, the pressure scale is

$$p_s = \rho_r U_r^2 = \gamma_r p_r M_r^2$$

which is representative of pressure differences in the flow. Thus, we have:

$$\frac{\Delta p}{p_r} \sim M_r^2$$

Hence, very low Mach number flows experience pressure differences which are much smaller than the absolute or thermodynamic pressure. This illustrates the dual role of pressure: the absolute pressure plays a thermodynamic role in the equation of state while pressure differences play a mechanical role in the momentum equations. The present pressure scaling ensures that the magnitude of the dimensionless pressure differences is of the order one. However, the dimensionless absolute pressure itself goes to infinity as the reference Mach number approaches zero.

An appropriate nondimensionalization for the pressure should provide magnitudes of order one for *both* the dimensionless pressure differences in the momentum equation *and* the dimensionless thermodynamic pressure in the equation of state. Meeting these conditions will improve the behavior of the numerical solution algorithm, and will ensure that the appropriate limiting form of the equations are recovered without indeterminacies. Simply stated, one must properly scale both the pressure and its gradient.

This is achieved by selecting appropriate values for both the pressure scale and its reference state:

$$\tilde{p} = \frac{p - p_r}{p_s} = \frac{p - p_r}{\rho_r U_r^2}$$

Eqs. (1)–(3) then take the following dimensionless form:

$$\begin{aligned}
&-\widetilde{\nabla}\cdot\tilde{\boldsymbol{u}} = \frac{\gamma_r M_r^2}{\gamma_r M_r^2\tilde{p}+1}\tilde{\boldsymbol{u}}\cdot\widetilde{\nabla}\tilde{p} - \frac{1}{\widetilde{T}}\tilde{\boldsymbol{u}}\cdot\widetilde{\nabla}\widetilde{T}\\
&\tilde{\rho}\tilde{\boldsymbol{u}}\cdot\widetilde{\nabla}\tilde{\boldsymbol{u}}\\
&\quad = -\widetilde{\nabla}\tilde{p} + \frac{1}{Re}\widetilde{\nabla}\cdot\left[\tilde{\mu}\left(\widetilde{\nabla}\tilde{\boldsymbol{u}} + \widetilde{\nabla}\tilde{\boldsymbol{u}}^{\mathrm{T}}\right) - \frac{2}{3}\tilde{\mu}\boldsymbol{I}\widetilde{\nabla}\cdot\tilde{\boldsymbol{u}}\right] + \tilde{\rho}\tilde{\boldsymbol{f}}\\
&\tilde{\rho}\tilde{c}_p\tilde{\boldsymbol{u}}\cdot\widetilde{\nabla}\widetilde{T}\\
&\quad = (\gamma_r - 1)M_r^2\tilde{\boldsymbol{u}}\cdot\widetilde{\nabla}\tilde{p} + \frac{1}{Re\,Pr}\widetilde{\nabla}\cdot\left(\tilde{\lambda}\widetilde{\nabla}\widetilde{T}\right) + \tilde{\rho}\tilde{q}_s\\
&\tilde{\rho} = \frac{\gamma_r M_r^2\tilde{p}+1}{\widetilde{T}}
\end{aligned} \tag{5}$$

There remains to verify that this form of the equations is well posed in the limit of zero Mach number and large temperature differences. The limit $M_r = 0$ applied to Eqs. (5) yields the following system of equations:

$$\begin{aligned}
&-\widetilde{\nabla}\cdot\tilde{\boldsymbol{u}} = -\frac{1}{\widetilde{T}}\tilde{\boldsymbol{u}}\cdot\widetilde{\nabla}\widetilde{T}\\
&\tilde{\rho}\tilde{\boldsymbol{u}}\cdot\widetilde{\nabla}\tilde{\boldsymbol{u}}\\
&\quad = -\widetilde{\nabla}\tilde{p} + \frac{1}{Re}\widetilde{\nabla}\cdot\left[\tilde{\mu}\left(\widetilde{\nabla}\tilde{\boldsymbol{u}} + \widetilde{\nabla}\tilde{\boldsymbol{u}}^{\mathrm{T}}\right) - \frac{2}{3}\tilde{\mu}\boldsymbol{I}\widetilde{\nabla}\cdot\tilde{\boldsymbol{u}}\right] + \tilde{\rho}\tilde{\boldsymbol{f}}\\
&\tilde{\rho}\tilde{c}_p\tilde{\boldsymbol{u}}\cdot\widetilde{\nabla}\widetilde{T} = \frac{1}{Re\,Pr}\widetilde{\nabla}\cdot\left(\tilde{\lambda}\widetilde{\nabla}\widetilde{T}\right) + \tilde{\rho}\tilde{q}_s\\
&\tilde{\rho} = \frac{1}{\widetilde{T}}
\end{aligned} \tag{6}$$

These are the so-called anelastic flow equations [18] which are appropriate for strongly heated flows. Density is a function of temperature only. Notice also that the pressure term in the continuity equation has vanished reflecting the fact that density changes are due to temperature only. Setting $M_r = 0$ induces no singularity or indeterminacy.

Let us now examine the well posedness of the system for the other limit: incompressible flow with constant properties. This situation arises when temperature differences are small and the Mach number is very low. Eqs. (6) contain the limit $M_r = 0$ but the equation of state does not explicitly reduce to that of incompressible flow ($\tilde{\rho} = 1$). The expected limit form of the equation of state can be recovered through an appropriate scaling of temperature. The situation is similar to that encountered previously with the scaling of pressure. Temperature differences are small compared to the absolute temperature. With the present scaling, the dimensionless temperature is of order one but its variations are very small. This prevents simplifications of the differential equations from occuring.

The cure consists in introducing both a reference state and a temperature scale to ensure that $\widetilde{T}$ and $\Delta\widetilde{T}$ are both of order one:

$$\widetilde{T} = \frac{T - T_r}{T_s}$$

Eqs. (1)–(3) then take the following form:

$$\begin{aligned}
&-\widetilde{\nabla}\cdot\tilde{\boldsymbol{u}} = \frac{\gamma_r M_r^2}{\gamma_r M_r^2\tilde{p}+1}\tilde{\boldsymbol{u}}\cdot\widetilde{\nabla}\tilde{p} - \frac{T_s/T_r}{T_s/T_r\widetilde{T}+1}\tilde{\boldsymbol{u}}\cdot\widetilde{\nabla}\widetilde{T}\\
&\tilde{\rho}\tilde{\boldsymbol{u}}\cdot\widetilde{\nabla}\tilde{\boldsymbol{u}}\\
&\quad = -\widetilde{\nabla}\tilde{p} + \frac{1}{Re}\widetilde{\nabla}\cdot\left[\tilde{\mu}\left(\widetilde{\nabla}\tilde{\boldsymbol{u}} + \widetilde{\nabla}\tilde{\boldsymbol{u}}^{\mathrm{T}}\right) - \frac{2}{3}\tilde{\mu}\boldsymbol{I}\widetilde{\nabla}\cdot\tilde{\boldsymbol{u}}\right] + \tilde{\rho}\tilde{\boldsymbol{f}}\\
&\tilde{\rho}\tilde{c}_p\tilde{\boldsymbol{u}}\cdot\widetilde{\nabla}\widetilde{T} = Ec\tilde{\boldsymbol{u}}\cdot\widetilde{\nabla}\tilde{p} + \frac{1}{Re\,Pr}\widetilde{\nabla}\cdot\left(\tilde{\lambda}\widetilde{\nabla}\widetilde{T}\right) + \tilde{\rho}\tilde{q}_s\\
&\tilde{\rho} = \frac{\gamma_r M_r^2\tilde{p}+1}{(T_s/T_r)\widetilde{T}+1}
\end{aligned} \tag{7}$$

where Ec is the Eckert number:

$$Ec = \frac{(\gamma_r - 1)M_r^2}{T_s/T_r}$$

Selecting proper reference states and scales that are truly representative of the physics is very important to avoid ill-posed systems. Here, a meaningful temperature scale T_s (i.e., representative of temperature differences) is the difference between the wall and ambient (reference) temperatures:

$$T_s = T_w - T_r$$

This choice is relevant for problems with a prescribed temperature difference that is comparable to or is large with respect to the isentropic temperature change. This would, of course, be an inappropriate choice for adiabatic flows.

Eqs. (7) are applicable to fully compressible flows. We can now focus on specific cases of interest in the present

study. The first one concerns very low Mach number flows: $M_r = 0$ which implies $Ec = 0$. Eqs. (7) reduce to:

$$
\begin{aligned}
&-\widetilde{\nabla}\cdot\tilde{\boldsymbol{u}} = -\frac{T_s/T_r}{T_s/T_r\widetilde{T}+1}\tilde{\boldsymbol{u}}\cdot\widetilde{\nabla}\widetilde{T}\\
&\tilde{\rho}\tilde{\boldsymbol{u}}\cdot\widetilde{\nabla}\tilde{\boldsymbol{u}}\\
&\quad = -\widetilde{\nabla}\tilde{p} + \frac{1}{Re}\widetilde{\nabla}\cdot\left[\tilde{\mu}\left(\widetilde{\nabla}\tilde{\boldsymbol{u}} + \widetilde{\nabla}\tilde{\boldsymbol{u}}^{\mathrm{T}}\right) - \frac{2}{3}\tilde{\mu}\boldsymbol{I}\widetilde{\nabla}\cdot\tilde{\boldsymbol{u}}\right] + \tilde{\rho}\tilde{\boldsymbol{f}}\\
&\tilde{\rho}\tilde{c}_p\tilde{\boldsymbol{u}}\cdot\widetilde{\nabla}\widetilde{T} = \frac{1}{Re\,Pr}\widetilde{\nabla}\cdot\left(\tilde{\lambda}\widetilde{\nabla}\widetilde{T}\right) + \tilde{\rho}\tilde{q}_s\\
&\tilde{\rho} = \frac{1}{(T_s/T_r)\widetilde{T}+1}
\end{aligned}
\tag{8}
$$

These equations are equivalent to system (6) and are appropriate for strongly heated (anelastic) flows. The other case of interest is incompressible flow with small temperature differences ($T_s/T_r = 0$). The present nondimensional form of the equations shows explicitly that density becomes constant. The limiting form of the equations is:

$$
\begin{aligned}
&-\widetilde{\nabla}\cdot\tilde{\boldsymbol{u}} = 0\\
&\tilde{\rho}\tilde{\boldsymbol{u}}\cdot\widetilde{\nabla}\tilde{\boldsymbol{u}}\\
&\quad = -\widetilde{\nabla}\tilde{p} + \frac{1}{Re}\widetilde{\nabla}\cdot\left[\tilde{\mu}\left(\widetilde{\nabla}\tilde{\boldsymbol{u}} + \widetilde{\nabla}\tilde{\boldsymbol{u}}^{\mathrm{T}}\right) - \frac{2}{3}\tilde{\mu}\boldsymbol{I}\widetilde{\nabla}\cdot\tilde{\boldsymbol{u}}\right] + \tilde{\rho}\tilde{\boldsymbol{f}}\\
&\tilde{\rho}\tilde{c}_p\tilde{\boldsymbol{u}}\cdot\widetilde{\nabla}\widetilde{T} = \frac{1}{Re\,Pr}\widetilde{\nabla}\cdot\left(\tilde{\lambda}\widetilde{\nabla}\widetilde{T}\right) + \tilde{\rho}\tilde{q}_s\\
&\tilde{\rho} = 1
\end{aligned}
\tag{9}
$$

which is the correct form for incompressible flows. The only possible anomaly is the presence of the term $\frac{2}{3}\tilde{\mu}\boldsymbol{I}\widetilde{\nabla}\cdot\tilde{\boldsymbol{u}}$. But since the continuity equation requires a divergence free velocity vector, this term will numerically vanish or at least be very small. Thus the appropriate incompressible flow equations are recovered even if this term is still active in the model. Finally, the limit ($T_s/T_r = 0$) yields:

$$\frac{T}{T_r} = \widetilde{T}\frac{T_s}{T_r} + 1 = 1$$

so that fluid properties (Table 1) are constant as expected:

$$\tilde{\mu} = \frac{\mu}{\mu_r} = 1, \qquad \tilde{\lambda} = \frac{\lambda}{\lambda_r} = 1, \qquad \tilde{c}_p = \frac{c_p}{c_{p_r}} = 1$$

Notice that the simultaneous limits $M_r = 0$ and $T_s/T_r = 0$ generate an indeterminacy for Ec. This special case must be studied carefully because the two limits ($M_r = 0$ and $T_s/T_r = 0$) are independent processes. The Eckert number is:

$$\frac{(\gamma_r - 1)M_r^2 T_r}{T_s} \to \frac{0}{0} \tag{10}$$

The physical interpretation of this term provides the basis to properly specify the input parameter, that is $Ec = 0$. For adiabatic walls, the temperature scale (the typical temperature differences) is that described by Panton [19]:

$$\Delta T_{\text{adiabatic}} \sim \frac{U_r^2}{c_{p_r}} = (\gamma_r - 1)T_r M_r^2$$

This is the numerator of Eq. (10). Hence, the Eckert number may symbolically be written as:

$$Ec = \frac{\Delta T_{\text{adiabatic}}}{\Delta T_{\text{imposed}}}$$

When the flow approaches incompressibility, T_s must be small to ensure that fluid properties are constant. Hence, $\Delta T_{\text{imposed}}$ is small. At the same time $\Delta T_{\text{adiabatic}}$ must be much smaller than $\Delta T_{\text{imposed}}$ to guarantee that temperature changes and heat transfer are driven by the prescribed Dirichlet condition and not by compressibility effects. This is accomplished by setting $Ec = 0$ in Eqs. (7) so that Eqs. (9) for incompressible flows are recovered.

In summary, the proposed formulation using appropriate scales and reference states for both temperature and pressure makes it possible to treat all flow regimes in a unified manner: fully compressible, anelastic, and incompressible. A single system of differential equations (7) is used and the input parameters (M_r, Ec, and T_s/T_r) define the specific flow regime. This is an elegant and effective approach to solve flows where the various regimes may occur in different parts of the flow. It also ensures that observed differences between various flows are due to differences in the mathematical models of the flow physics rather than to differences in the numerics. The formulation has been demontrated for incompressible flows [11], inviscid and laminar compressible internal flows [11] and for inviscid, laminar and turbulent transonic flows over airfoils [12,20]. Finally, as will shown later, the formulation applies also to cases for which the flow is compressible in some region of the domain, anelastic in another, and incompressible in a third part of the flow domain.

The key feature of the formulation of the equations is that it makes explicit the dual role of pressure. It plays a mechanial role in the momemtum equation (pressure gradient) and a thermodynamic role in the equation of state (density variations due to pressure). The two pressure levels are scaled according to their respective role in the equations, thus removing possible indeterminacies of more standard formulations. Similar observations also hold for the dual role of temperature in the energy and momentum equations.

The formulation is valid for all-speed flows, including transonic and supersonic regimes. However, the numerical scheme used here may not be optimal for all flow regimes. Indeed, while the resulting pressure-based algorithm ensures incompressibility, it will satify the Hugoniot shock condition up to truncation error level. Density-based solvers use conserved variables and yield exact shock strength and speed. However, they cannot yield incompressible flows due to the presence of indeterminacies in the limit of vanishing *Mach* number.

The use of mesh adaptation in conjunction with the proposed formulation results in a pressure-based solver applicable to a broad spectrum of flow regimes (from incompressible to transonic) with excellent levels of accuracy [20].

2.3. Solution algorithm

The problem is solved using a standard Galerkin finite element method. The variational equations are obtained by multiplying each equation by a test function and integrating over the computational domain. The pressure gradient and viscous conduction terms are integrated by parts to provide natural boundary conditions. The weak form obtained is detailed in our previous work [12].

The system of equations is fully coupled and highly nonlinear, especially when density and properties vary. The continuity-momentum-energy system is solved in a fully coupled manner, using Newton's method. The discretization uses a quadratic velocity field, a quadratic temperature and a linear continuous pressure approximation on each finite element.

3. Adaptive methodology

The adaptive remeshing procedure is modeled after that of Peraire et al. [21] and is described in more details by Ilinca and Pelletier [12]. The procedure clusters grid points in regions of rapid variations of all dependent variables. Error estimates are obtained for velocity, pressure and temperature by a local least squares reconstruction of the solution derivatives [22,23]. Following our previous work [12], we consider the derivatives and not the fluxes. We omit the diffusion coefficient because properties vary with temperature so that element diffusion fluxes are no longer linear and discontinuous. For the velocity field, the term $\widetilde{\nabla}\tilde{\boldsymbol{u}} + \widetilde{\nabla}\tilde{\boldsymbol{u}}^{\mathrm{T}} - \frac{2}{3}\boldsymbol{I}\widetilde{\nabla}\cdot\tilde{\boldsymbol{u}}$ is used for error estimation. An error estimate for pressure is obtained by a local projection of the pressure itself. Error estimates are obtained for temperature by projecting its finite element derivatives into a continuous field.

Once the error estimates are obtained for all variables, a better mesh must be designed. In our approach all variables are analyzed and contribute to the mesh adaptation process. For this, an error estimate is obtained separately for each dependent variable. The mesh characteristics (element size) on a given element are derived for each variable. The minimum element size predicted for each of the dependent variable is selected on each element. Details of this algorithm have been presented previously [12,24,25].

4. Verification

The methodology is first verified on a problem possessing a closed form solution. This problem is designed to mimic a compressible laminar round jet impinging on a heated flat plate (see Fig. 1). It is a modified version of the incompressible analytical problem presented by Turgeon et al. [15]. The exact solution, in dimensionless form, is given by:

$$\tilde{p} = \mathrm{e}^{-400(\tilde{x}^2+\tilde{r}^2)}$$

$$\widetilde{T} = \mathrm{e}^{\frac{200\tilde{x}}{1+4\tilde{r}^2}}$$

$$\tilde{\rho} = \frac{\gamma_r M_r^2 \tilde{p} + 1}{(T_s/T_r)\widetilde{T} + 1}$$

$$\tilde{u} = 100\tilde{x}^2\left(\mathrm{e}^{-\tilde{x}^2\tilde{r}^2} - \mathrm{e}^{-0.01}\right)/\tilde{\rho}$$

$$\tilde{v} = -100\tilde{x}\tilde{r}\left(\mathrm{e}^{-\tilde{x}^2\tilde{r}^2} - \mathrm{e}^{-0.01}\right)/\tilde{\rho}$$

The physical properties are temperature dependent and vary according to the following expressions:

$$\tilde{\mu} = \left(\frac{T}{T_r}\right)^{0.68} = \left(\frac{T_s}{T_r}\widetilde{T} + 1\right)^{0.68}$$

$$\tilde{c}_p = \left(\frac{T_s}{T_r}\widetilde{T} + 1\right)^{0.05}$$

$$\tilde{\lambda} = \left(\frac{T_s}{T_r}\widetilde{T} + 1\right)^{0.76}$$

They correspond to the correlations of Table 1 for air. Finally, we set $Re = 100$, $Pr = 0.7$, $M_r = 0.7$, and $\gamma_r = 1.4$. The reference values are taken at the inlet and $T_s/T_r = 1$ ($T_w/T_r = 2$). Appropriate source terms $\boldsymbol{f}$ and q_s are obtained by substituting the above expressions into the Navier–Stokes and energy Eqs. (7).

The geometry is shown on Fig. 1. The curved boundary corresponds to a streamline where the velocity vanishes. Symmetry conditions are applied on the axis while Dirichlet conditions are applied everywhere else, except for a small portion of the vertical wall near the outlet where the radial velocity and the axial traction are set to zero. This boundary condition may seem counter intuitive, but it is exact for the problem at hand and provides the required pressure level ($\tilde{p} = 0$ there).

The adaptive strategy is set to reduce the error by a factor of two at each cycle of adaptation. We account for errors in velocity and temperature, but not in pressure. This choice is based on observations. First, numerical experiments have demonstrated that adaptation on pressure increases the number of nodes and improves the accuracy

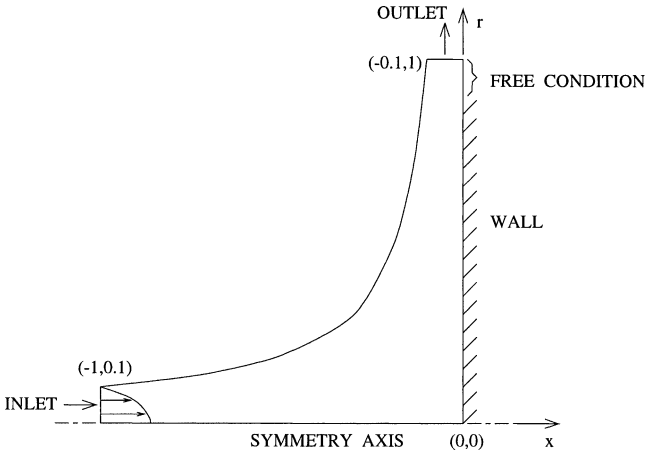

Fig. 1. Geometry for the analytical jet.

of pressure without significantly affecting the accuracy of either velocity or temperature. Furthermore, on all meshes the pressure error is small compared to the other errors. Thus, it is not necessary to adapt on pressure until the other sources of errors have been reduced to a comparable level. In any case, the velocity is strongly coupled to pressure and *feels* the errors in pressure in those regions where pressure varies rapidly. Finally, we are mostly interested in the flow and heat transfer predictions on the plate. Predictions of *Nu*, for instance, will be more accurate if we do not spend computational resources on pressure in regions which do not affect the flow very much. In practice, the pressure error is monitored to ensure its accuracy and to verify the performance of the error estimator.

Cartesian norms (instead of natural axisymmetric norms) are used for the errors. Turgeon and Pelletier [15] have already reported the advantages of doing so for such problems. Briefly, the adaptation attempts to *equidistribute* the *norm* of the error on each element. For axisymmetric problems, the natural norm is of the form:

$$\int \star\, r \,\mathrm{d}r \,\mathrm{d}x$$

The direct effect of r in the norm is that errors located away from the axis weigh more heavily in the new mesh design than those located near the axis. Thus, if the error norm is equidistributed, the derivative (*Nu* for instance) will be less accurate near the axis. In practice, one is interested in uniformly accurate values of the local Nusselt number. This is better achieved using a cartesian norm (without the r) which amounts to equidistribution of the average pointwise error.

Figs. 2 and 3 present the final mesh and solution. Note that the thermal boundary layer is much thinner than the hydrodynamic boundary layer.

The temperature distribution is thus much more difficult to capture accurately than the velocity field. However, the smoothness of contours provides visual cues of the solution accuracy. Clearly, the mesh is well adapted to the solution. It is most refined near the wall due to the large temperature gradients. Away from the wall, the mesh is quite regular because the velocity and temperature fields are very smooth. Note also the mesh clustering near the stagnation point. Even if the pressure error did not enter explicitly in the mesh adaptation, the mesh was sufficiently refined in this region to produce accurate prediction of all variables. The mesh characteristics are summarized in Table 2. The number of nodes doubles at each adaptive cycle indicating second order accuracy for velocity and temperature derivatives.

Fig. 4 shows the evolution of the error during the adaptive process. It decreases with mesh refinement indicating that the numerical solution converges to the exact solution. The relative error (ratio of the error norm to that of the solution) on the final mesh is about 0.1% for velocity, 0.8% for temperature, and 0.1% for pressure. Thus, the solution is very accurate even for derivatives (recall that error norms for temperature and velocity involve their first derivatives). As expected, the temperature gradient is less accurate than that of velocity. Finally, note that the behavior of the pressure error shows more irregularity than either velocity or temperature. This is primarily due to the fact that mesh adaptation does not explicitly account for errors in pressure. However, the accuracy of the pressure field improves with mesh refinement.

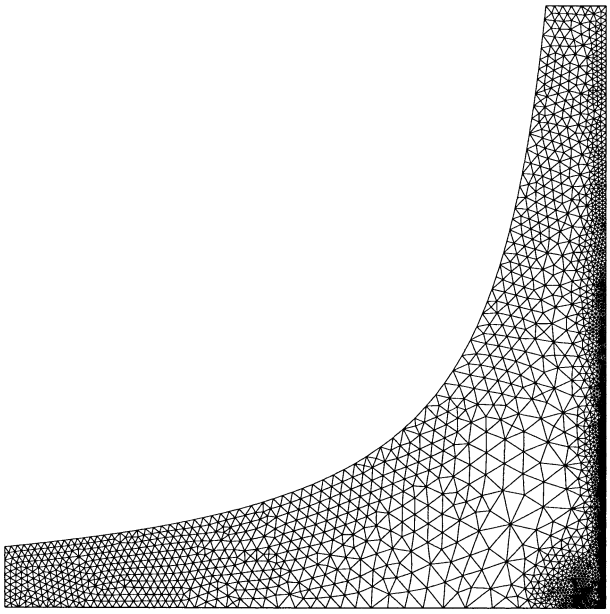

Fig. 2. Analytical jet: Final mesh.

Table 2
Meshes for the analytical jet

Adaptive cycle	Number of nodes	Number of elements
0	521	224
1	784	351
2	1348	615
3	2672	1249
4	5615	2670
5	10338	4981

While the accuracy of the solution is very important, that of the error estimator is also of interest. As we have just seen adaptation improves solution accuracy. Adaptivity also improves the accuracy and reliability of the error estimator. This reinforces confidence in the error estimator for real flows. As can be seen from Fig. 4, the error estimate is close to the true error. Moreover, the accuracy of the error estimate improves with adaptive mesh refinement. On the final mesh, the global efficiency index (ratio of the global error estimate to the true error) is higher than 93% for the three variables. The local efficiency index on individual elements is above 90% for those elements having an error larger than 3% of the average elemental error. The exception is for elements located on the boundary and for two isolated elements in the domain. The performance of the error estimator is known

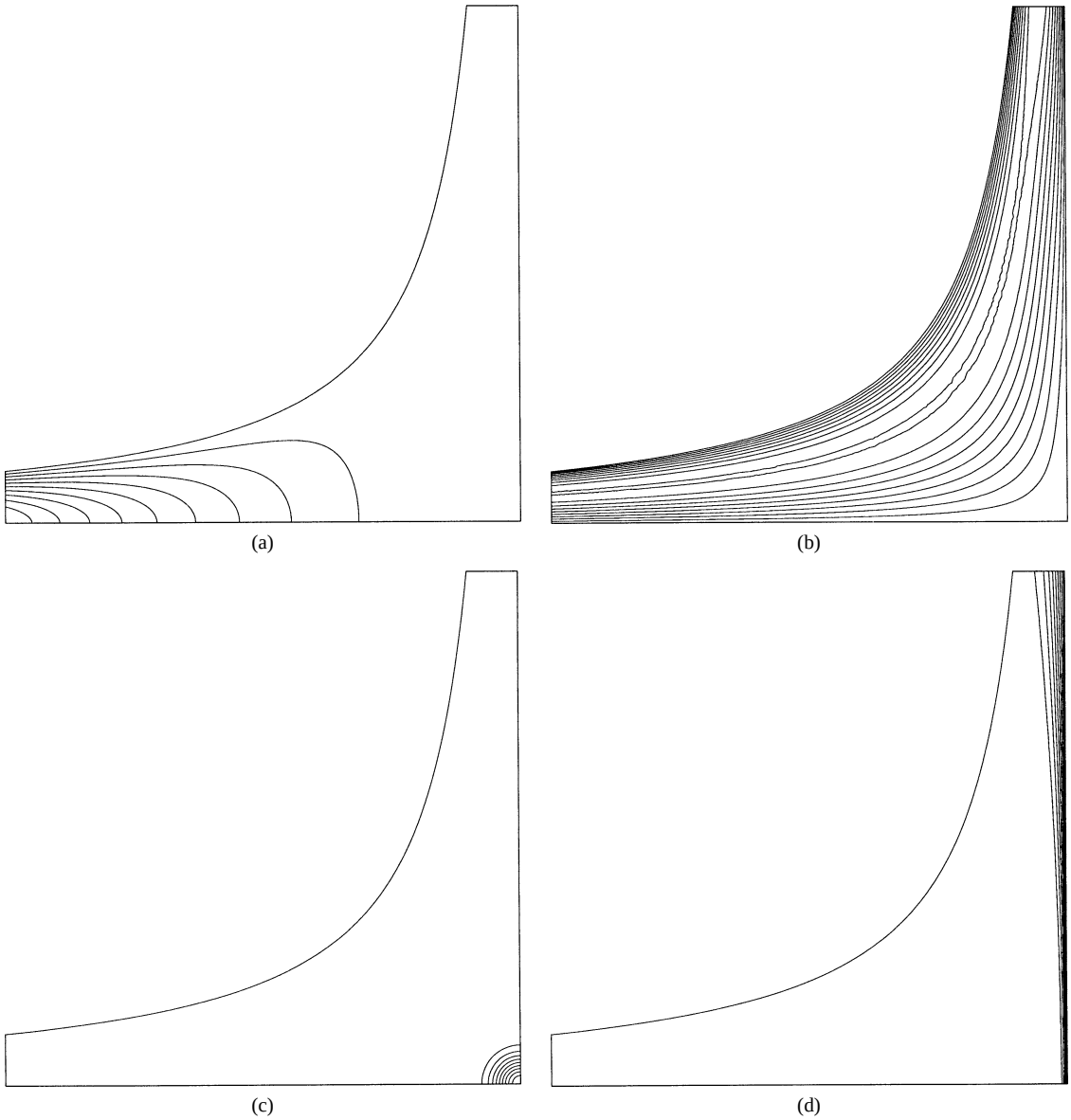

Fig. 3. Analytical jet: Final solution: (a) u/U_r; (b) v/U_r; (c) $(p - p_r)/\rho_r U_r^2$; (d) $(T - T_r)/(T_w - T_r)$.

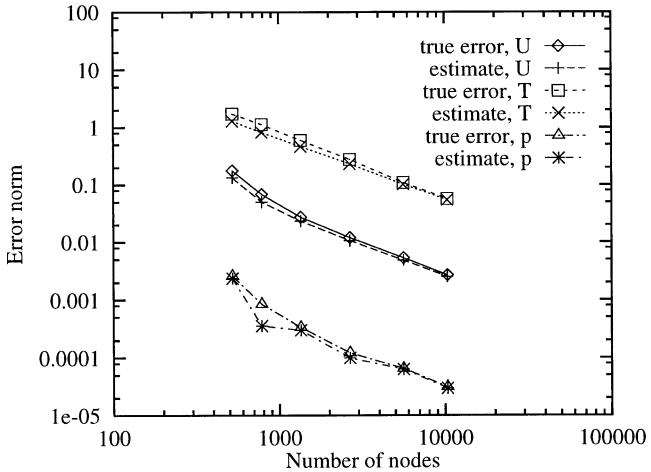

Fig. 4. Analytical jet: Trajectory of the error.

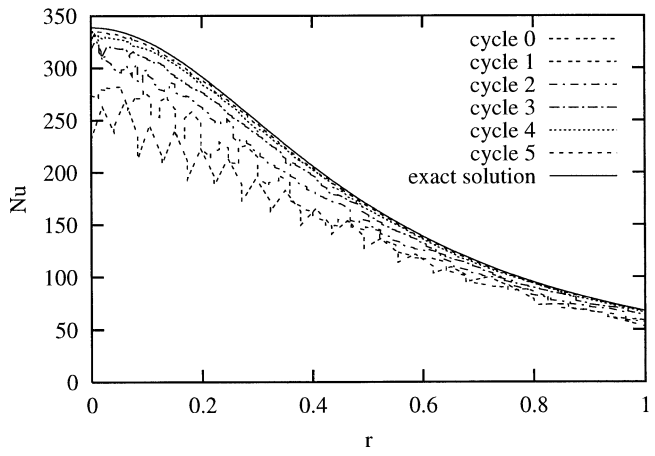

Fig. 5. Analytical jet: Nusselt number.

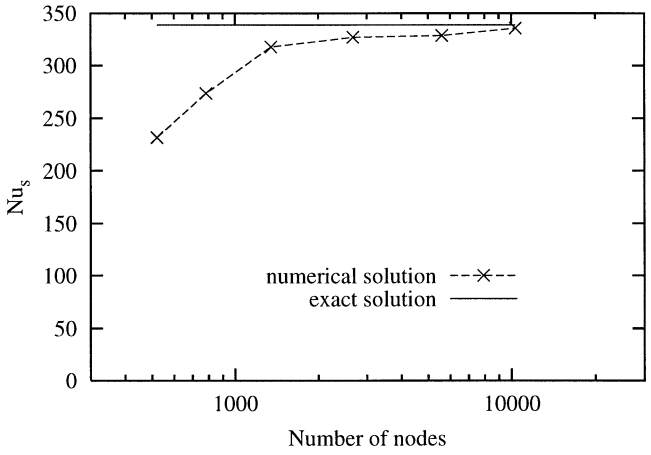

Fig. 6. Analytical jet: Stagnation Nusselt number.

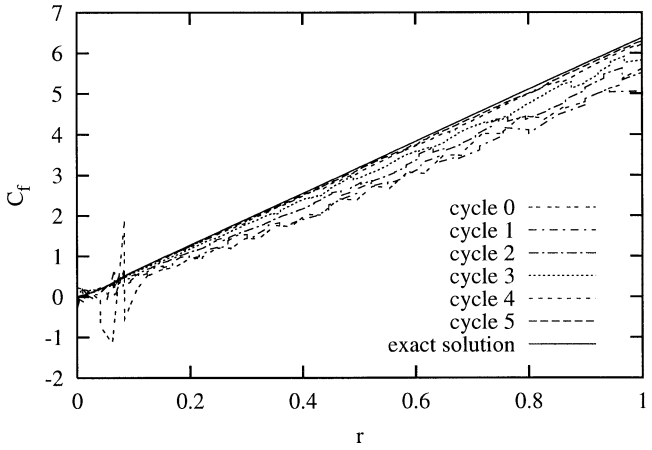

Fig. 7. Analytical jet: Skin friction.

to be poorer near boundaries due to a lack of neighboring information for the projection.

Let us now look at the accuracy of the Nusselt number, the natural measure of heat transfer at the wall. The local Nusselt number (based on the fluid properties evaluated at a reference temperature T_r) is defined as

$$Nu = \frac{q_w L_r}{\lambda_r (T_w - T_\infty)}$$

where q_w is the heat flux, L_r is the characteristic length, and T_∞ is the inlet temperature (which is equal to the reference temperature T_r). The subscript w stands for conditions at the wall. Since the problem is solved in dimensionless form, *Nu* reduces to

$$Nu = \frac{\lambda_w}{\lambda_r}\left(\frac{\partial \widetilde{T}}{\partial \tilde{x}}\right)_w = \tilde{\lambda}_w \left(\frac{\partial \widetilde{T}}{\partial \tilde{x}}\right)_w$$

The Nusselt number distribution along the plate is shown on Fig. 5. Predictions on the first meshes are poor, but they improve with mesh refinement. The numerical solution clearly converges to the exact solution (solid line) indicating that adaptivity can produce grid independent solutions. The region near the axis of symmetry ($r = 0$) experiences the largest errors due to the extreme thinness of the thermal boundary layer.

Fig. 6 presents another illustration of the grid convergence of *Nu*: the evolution of the stagnation point Nusselt number, Nu_s, with mesh refinement. The conditions at the stagnation point are very severe (the maximum temperature gradient occurs there). Clearly, Nu_s improves with mesh refinement and converges to the exact solution. On the final mesh, the error on Nu_s is less than 0.9%. Thus adaptivity has produced an accurate solution.

Fig. 7 presents the distribution of the skin friction coefficient C_f along the plate:

$$C_f = \frac{\tau_w}{\frac{1}{2}\rho_r U_r^2}$$

or in the dimensionless form

$$C_f = \frac{-2}{Re}\frac{\mu_w}{\mu_r}\frac{\partial \tilde{v}}{\partial \tilde{x}}$$

The negative sign ensures a positive value for C_f. Here again, the small differences between predictions on the last two adaptive meshes show that the adaptive methodology has produced a grid independent solution. Furthermore, the skin friction coefficient converges to its exact distribution.

This verification exercise has shown that the proposed adaptive methodology can accurately solve compressible laminar flows with heat transfer and temperature dependent fluid properties. Even the very thin thermal boundary layer is predicted accurately. The error estimator also provides a good approximation of the real error, both globally and locally. We can now proceed with increased confidence to the solution of real problems presenting a similar level of complexity.

There are several ways to evaluate the *Nusselt* number and the skin friction coefficients: direct differentiation of the finite element solution, use of the projected derivatives computed in the error estimation process [22,23] or post-processing techniques based on equilibrium arguments [26–28]. Derivatives of the finite element solutions have been used here for several reasons. First, the method is simple to implement and general. Second, commercial software often compute derived quatities in this manner. Hence, our results offer clues as to the fineness of meshes required to achieve grid converged results with commercial tools. It is understood that more sophisticated methods of derivative extractions would require fewer cycles of mesh adaptation to achieve grid converged *Nusselt* number and skin friction distributions. However, the overal approach would remain unchanged.

5. Applications

The adaptive methodology is now applied to the solution of real impinging jets. First, we consider very low Mach number flows with temperature dependent fluid properties. Two gases (air and CO_2) and three different flow conditions (very hot wall, very cold wall, and small temperature

differences) are considered. Fully compressible jets at high subsonic Mach number are then studied.

5.1. Very low Mach number jets—problem definition

The first part of the study focuses on anelastic flows with temperature dependent fluid properties. The problems selected correspond to those described by Aihara et al. [17]. Note that no experimental data are available. These low velocity flows ($M_r = 0$) experience large temperature variations so that fluid properties cannot be considered constant. Density is a function of temperature only and the governing equations (7) reduce to Eqs. (8) with no source terms.

The computational domain for all cases is shown on Fig. 8 (not to scale). It extends $15d$ from the axis in the radial direction and $4d$ upstream of the jet lips. The distance between the jet lips and the wall is $2d$ and the entrance tube is $2d$ long. The tube thickness is considered small and set to $0.02d$. A parabolic velocity profile is imposed at the inlet. At the outlet (upper boundary, $r/d = 15$) the radial traction and the axial velocity are set to zero. On the entrainment boundary (to the left), the axial traction and radial velocity are set to zero. The inlet temperature is uniform and equal to the ambient temperature at the entrainment boundary ($\widetilde{T} = 0$). The normal derivative of temperature at the outlet and tube surface is set to zero. The wall is maintained at a constant temperature, $\widetilde{T} = 1$. Finally, $T_r = 600$ K and $T_s = -300$ K for the hot jet on a cold wall, while $T_r = 300$ K and $T_s = 300$ K for the cold jet on a hot wall.

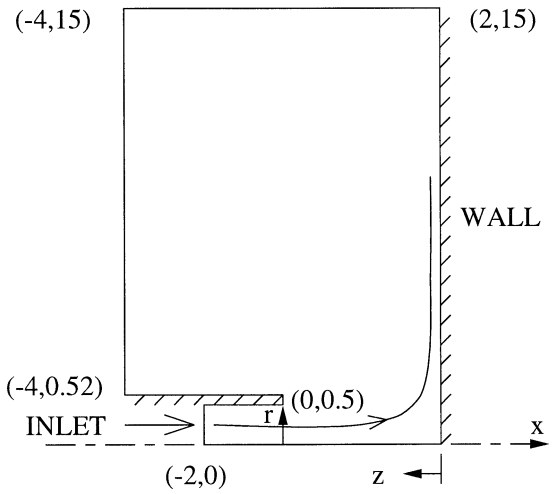

Fig. 8. Geometry for the real jet.

Table 3
Prandtl numbers

gas	Pr at $T_r = 300$ K	Pr at $T_r = 600$ K
air	0.71	0.69
CO_2	0.78	0.75

The Reynolds number based on the inlet diameter d, mean velocity U_r, and reference properties ρ_r and μ_r is 500 for all the problems studied. The Prandtl number depends on the gas used and the inlet temperature. Its values are listed in Table 3. The temperature dependence of the fluid properties are given in Table 1. Finally, the adaptive methodology is set to reduce the error in temperature and velocity by a factor 2 at each adaptive cycle. The following subsections present numerical results.

5.2. Air jet on a hot wall

The first application is for a very low Mach number jet of air impinging on a hot wall ($M_r = 0$, $T_w/T_r = 2$). This example is used to illustrate the general behavior of the impinging jet and to assess the performance of the adaptive methodology.

Figs. 9 and 10 presents the final mesh and solution. The contours of axial and radial velocities illustrate the flow physics: the jet hits the wall and is deflected radially. A boundary layer develops along the wall; the radial velocity reaches a maximum and then decreases progressively to lower values as r increases. Pressure variations are confined to the stagnation point region while temperature exhibits a very thin boundary layer. Globally, the smoothness of contour lines provides visual cues of the solution accuracy. Finally, the mesh is efficiently refined, with smaller elements where the solution gradients are large. Notice the refinement in the boundary layer: element size increases with boundary layer thickening. The shear layer emanating from the jets lips also leads to mesh refinement. Observe that the mesh is refined in the region of high pressure gradients even if adaptivity did not explicitly account for errors in pressure. The a priori generation of such a well adapted mesh is nearly impossible without adaptivity.

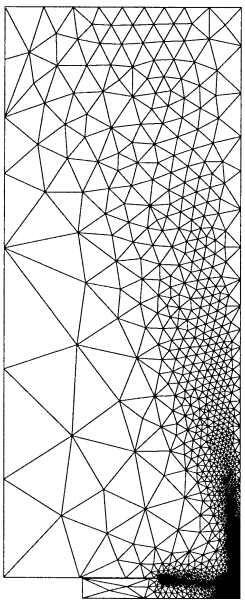

Fig. 9. Airjet: Final mesh.

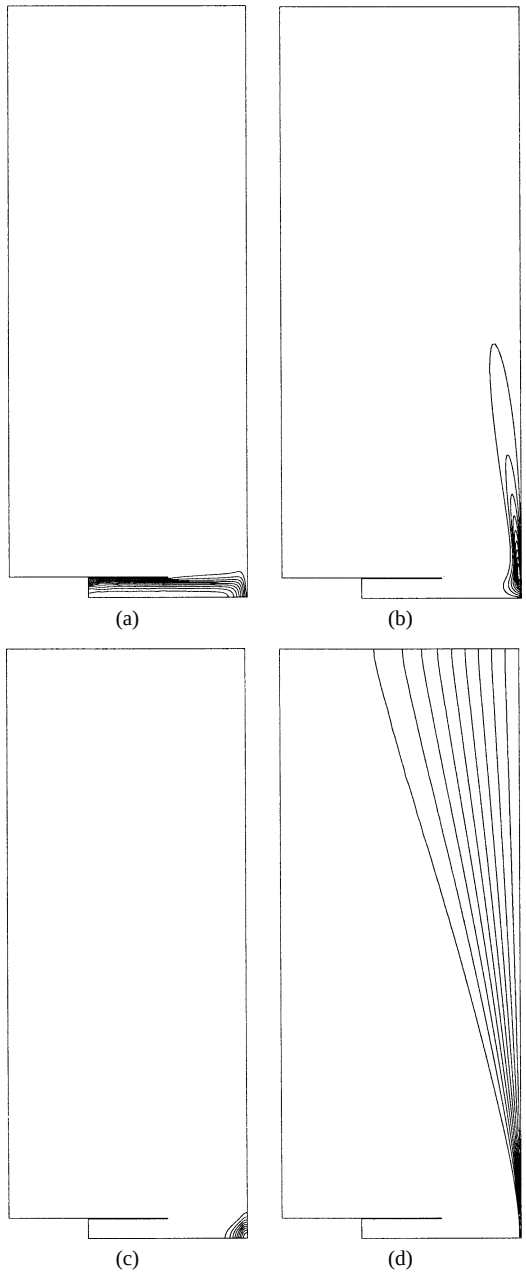

Fig. 10. Air jet on hot wall: Solution on final mesh: (a) u/U_r; (b) v/U_r; (c) $(p - p_r)/\rho_r U_r^2$; (d) $(T - T_r)/(T_w - T_r)$.

The distribution of the local Nusselt number is presented in Fig. 11 for $0 \leqslant r/d \leqslant 3$, the range of most interest in practice. Predictions are poor on the first two meshes but clearly converge to a well defined limit as the mesh is refined. The stagnation Nusselt number Nu_s varies by 1% between cycles 2 and 4 and by less than 0.1% between cycles 3 and 4. The solution is thus grid converged and very accurate. The estimated relative error is 0.8% in velocity, 0.4% in temperature, and 0.1% in pressure on the final mesh. Only four cycles of adaptation were needed to produce a final mesh with 9557 nodes.

Fig. 12 shows the distribution of the skin friction coefficient along the plate. Physically, the skin friction coefficient

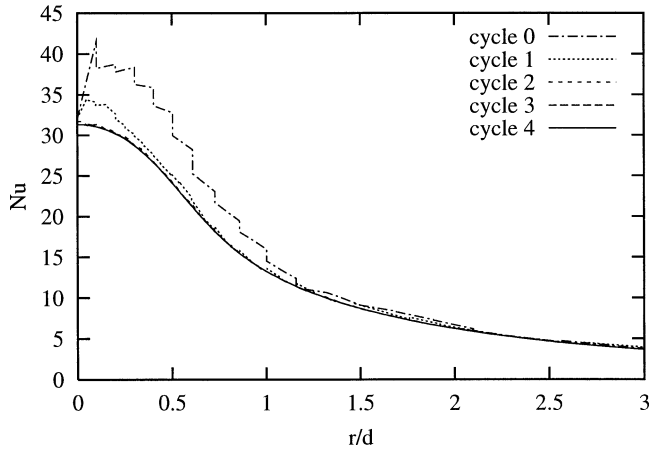

Fig. 11. Air jet on hot wall: Nusselt number.

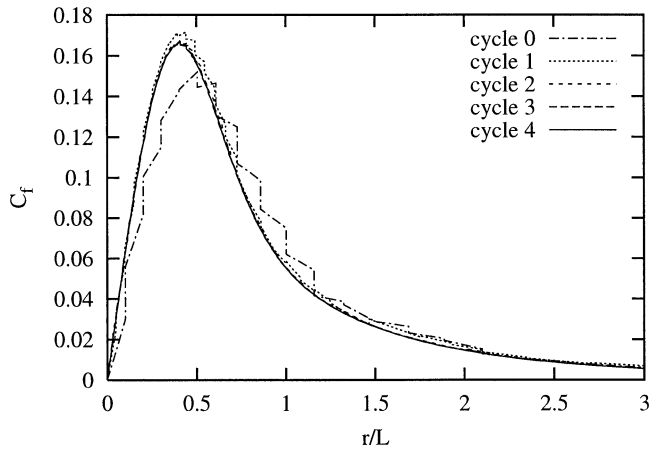

Fig. 12. Air jet on hot wall: Skin friction.

vanishes at $r/d = 0$ due to symmetry; it increases to a maximum value, at a position close to that of the maximum value of the radial velocity, and then decreases rapidly with the thickening of the boundary layer. Here again, the solution converges to a clear limit. The small differences in C_f between the final adaptive cycles indicate that the solution is grid converged and accurate.

5.3. Air jet

The previous application has illustrated the physics of the problem and the high accuracy provided by the adaptive methodology. We now study different heat transfer configurations for an air jet: a hot wall ($T_w/T_r = 2$), a cold wall ($T_w/T_r = 0.5$), and flow with constant fluid properties. For the case with constant properties, the inlet temperature is the same as that for the hot wall jet, that is, $Pr = 0.71$. Eqs. (7) reduces to (9) for this case. The adaptive strategy was applied in turn to each case. For simplicity and clarity only the final, grid converged solutions are compared. Solutions for intermediate meshes are not reported.

Fig. 13 presents the distribution of *Nu* along the plate for all cases. Each case uses its own mesh sequence generated

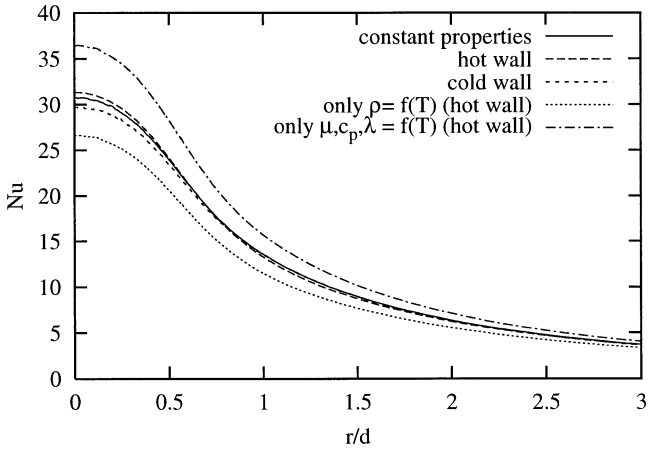

Fig. 13. Air: Nusselt number.

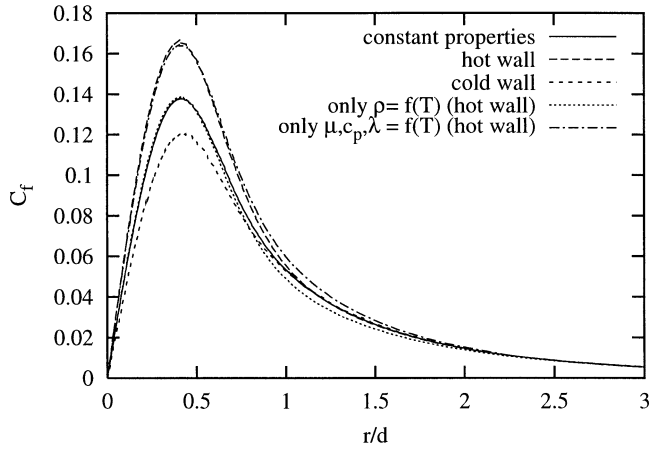

Fig. 14. Air: Skin friction.

from its own error analysis. The heating or cooling appears to have little influence on *Nu*. It is slightly higher when the wall is hot, intermediate with constant properties, and lower for a cold wall. This does not mean that the solutions are very close: the temperature *gradients* are quite different because the properties differ significantly. For constant properties, the solution is independent of the heating or cooling of the wall. The apparently low sensitivity of the solution to temperature dependence of the fluid properties is due to the fact that variations in density and other physical properties have opposite effects on the Nusselt number that almost cancel each other. Fig. 13 also shows results obtained for the hot wall when the temperature dependence of density is considered separately from those of the other fluid properties. When density is kept constant and μ, c_p, and λ are allowed to vary, *Nu* increases more significantly. Conversely, if density is the only property allowed to vary, *Nu* is quite lower. The two trends nearly cancel each other when all properties are allowed to vary.

Fig. 14 shows the local skin friction coefficient distribution on the wall for the same five cases. The influence of the wall condition (hot, cold or small temperature differences) is more pronounced. C_f is larger when the jet is heated by the wall. This seems to be related to an increase of viscosity with temperature. In fact, if one looks at the cases of constant density and constant values for the other properties, one concludes that the effect of ρ is small but that those of the other properties, is larger: incompressible and compressible jets with constant properties are almost identical while predictions from variable property models for a hot wall are extremely close together.

5.4. CO_2 *jet*

The case of a carbon dioxide (CO_2) jet is studied since it is more interesting due to the larger variations of its physical properties. It provides a more demanding test case for the adaptive finite element algorithm. Again, we consider three cases: hot wall, cold wall, and constant properties. The latter is slightly heated, with an inlet temperature of 300 K, the same temperature as for the fully heated case. Figs. 15 and 16 present the distributions of *Nu* and C_f. Grid independent solutions are obtained in 4 to 6 cycles of adaptation. The effects of the wall temperature are similar to those observed for air, but are more pronounced. The wall temperature has a more significant effect on the Nusselt number than it did for air.

5.5. *Compressible air jet*

Next, complexity of the problem is increased by including compressibility effects due to pressure (Mach number effects). The previous problem is solved again, but this time with $M_r = 0.5$. This choice deserves some comments. First, the Reynolds number is kept at 500. This condition will occur for very small geometries (small length scale L_r). It also allows for a direct comparison with low Mach number results. Also, the inlet velocity profile is again parabolic. It is realistic even at high subsonic M_r because *Re* is low (important viscous effects). Note that the reference velocity is the mean inlet velocity, thus the inlet Mach number distribution is parabolic with a maximum of 1. Finally, the inlet tube is reduced to a smaller length ($0.2d$) to avoid temperature drops which would make comparisons to low Mach number solutions more difficult. The study is restricted to air. The governing equations are given by system (7) and the fluid properties vary according to the expressions given in Table 1.

The choice of the reference state also deserves some comments. The natural reference velocity is based on the inlet conditions, here the mean inlet velocity. A well posed problem requires that both the inlet and ambient temperatures be given. We assume that they are equal. Fluid properties at the inlet and ambient conditions are thus identical. However the only known pressure is the ambient pressure. Choosing this value for the reference state makes it possible (and convenient) to apply a zero normal traction condition (i.e., $\tilde{p} = 0$) at the outlet and entrainment boundaries. Thus, the ambient pressure, temperature and density are used as reference state, even though it may not be the obvious or natural choice.

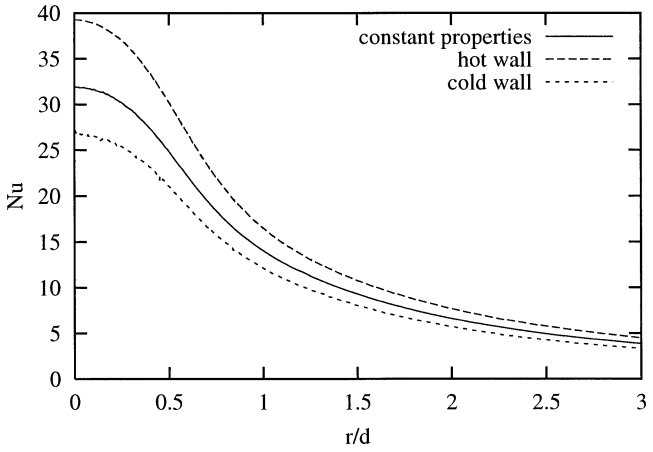

Fig. 15. CO_2: Nusselt number.

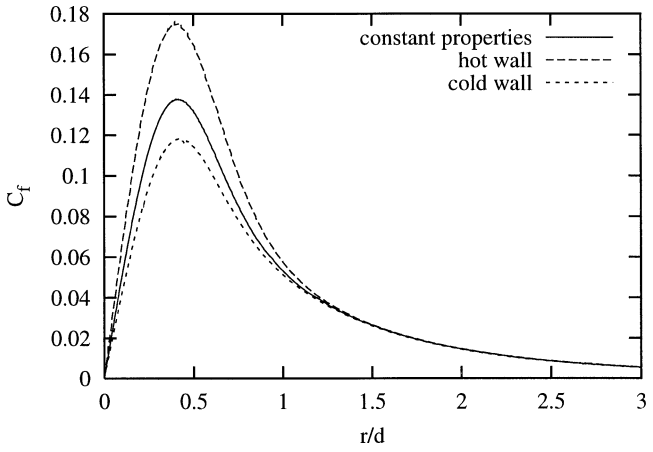

Fig. 16. CO_2: Skin friction.

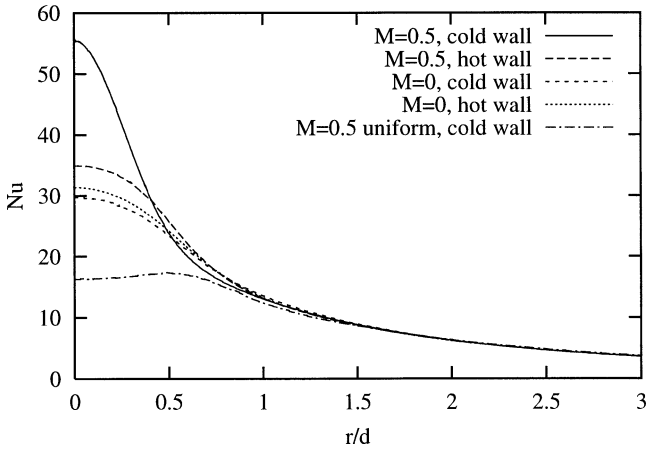

Fig. 17. Air at $M = 0.5$: Nusselt number.

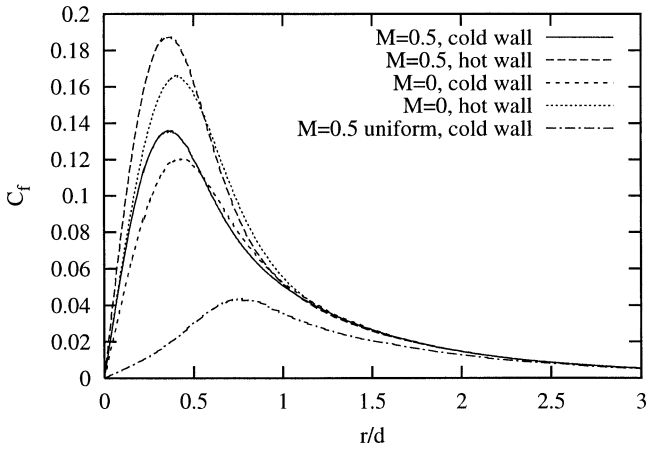

Fig. 18. Air at $M = 0.5$: Skin friction.

The consequence is that the Reynolds number, which is based on these reference values, has a slightly different interpretation than a *Re* based on the inlet conditions. Comparisons of results are best achieved if conditions defining the Reynolds number are the same for all configurations. It is not the case here. However, careful study of numerical predictions indicates that the inlet pressure and density are nearly equal to the ambient values. Thus, the Reynolds numbers based on the inlet or ambient conditions are, for all practical purposes, identical. Finally, the question of the Mach number is clear cut: M_r depends on velocity and temperature (U_r and T_r) only, which are well defined at the inlet. The Mach number is thus really representative of the inlet conditions.

Computations were performed for both hot and cold walls. Again, *Nu* and C_f are used for comparing predictions. Fig. 17 presents the local Nusselt number distribution obtained on the final mesh. Results at $M_r = 0$ are included for comparison. The fifth curve, which corresponds to a uniform inflow velocity, will be discussed later. As can be seen compressibility significantly increases *Nu* for both heated and cooled jets. This is especially evident near the stagnation point ($r = 0$). For the cold wall case, Nu_s is nearly doubled and is higher than that for the hot wall case. Predictions for all cases are very close for $r/d > 1.5$ indicating that compressibility effects are confined to the stagnation point region.

Fig. 18 provides the local skin friction coefficient distribution along the wall. Compressibility increases the level of C_f for both cases. The location of the maximum is also closer to the axis of symmetry.

Including compressibility effects also increases the demands on the flow solver. As can be seen on Fig. 17, *Nu* increases due to compressibility. This is accompanied by an increase of the temperature gradient making this problem more difficult to solve. The cold wall problems are also more demanding. For the same *Nu*, the conductivity $\tilde{\lambda}_w$ is lower for a cold wall than for a hot wall. Hence, the temperature gradient at the wall is larger for the cold wall than the hot wall. The hydrodynamic boundary layer is also thinner for a cold wall because the apparent viscosity is lower. For example, $\widetilde{\nabla}\widetilde{T}$ is 5 times higher for the air jet on a cold wall at $M_r = 0.5$ than for the air jet on a hot wall at $M_r = 0$. To illustrate this harder condition, Fig. 19 shows the convergence of *Nu* with mesh refinement for air jet on a cold wall at $M_r = 0.5$. As expected, more adaptive cycles and more nodes are needed to achieve a grid independent solution at

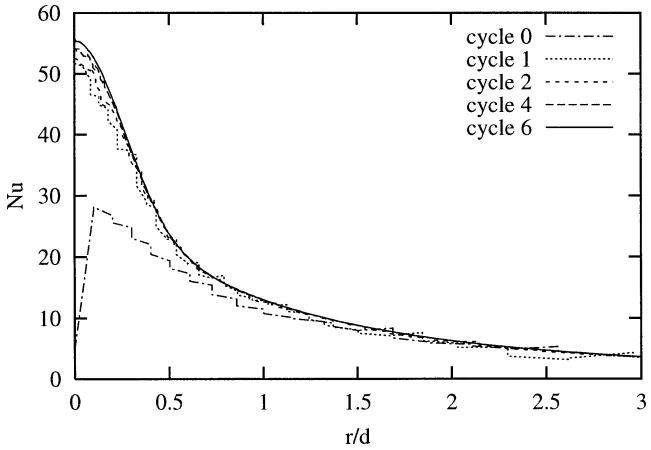

Fig. 19. Aircon cold wall, $M = 0.5$: Nusselt number.

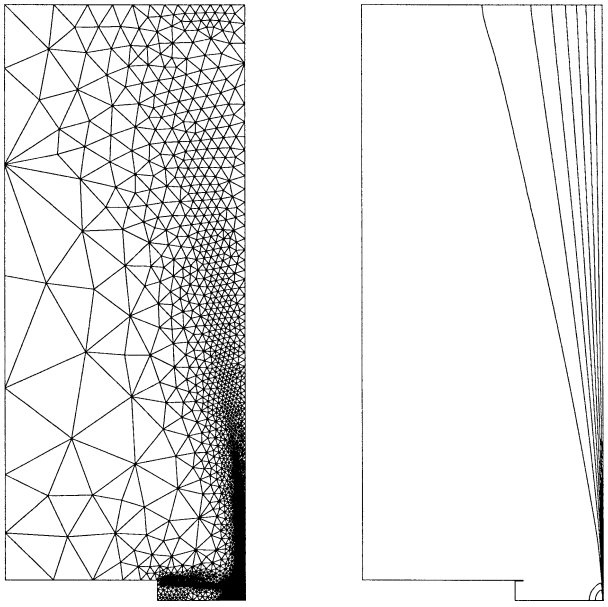

Fig. 20. Air on cold wall, $M = 0.5$: Final mesh and solution: (a) mesh; (b) $(T - T_r)/(T_w - T_r)$.

higher Mach numbers. This should be contrasted with the results of Fig. 11 for very low Mach numbers. The greater severity of this problem can also be observed on Fig. 20.

The thermal boundary layer is thinner at $M_r = 0.5$ than at $M_r = 0$ (see Fig. 10). It is even thinner in the region near the symmetry axis (not shown here). But the methodology is still very cost-effective, yielding an accurate solution for this harder problem.

Comparison of Figs. 10 and 20 reveals an interesting difference: at high subsonic Mach number there is a temperature increase upstream of the stagnation point due to compressibility. Fig. 21 shows the temperature distribution on the symmetry axis near the wall. The temperature increases significantly before decreasing to the cold wall value. The temperature rise is very close to the theoretical isentropic temperature rise which was computed using the total temperature at $x/d = 1.2$, the local Mach number provided by the numerical solution, and the relation:

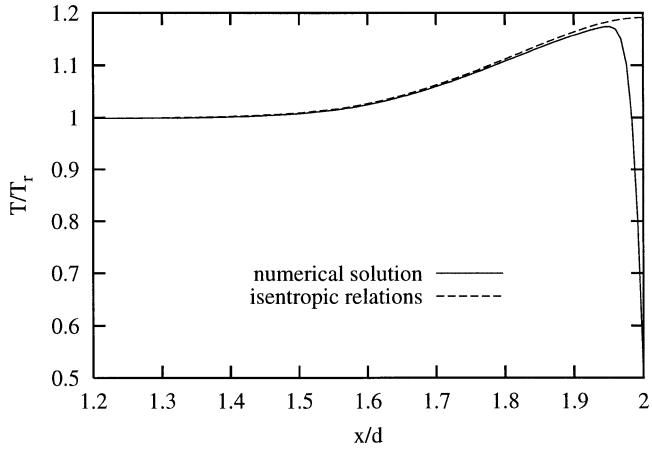

Fig. 21. Temperature rise due to compressibility effects.

$$\frac{T}{T_{\text{tot}}} = \left(1 + \frac{\gamma - 1}{2} M^2\right)^{-1}$$

with $\gamma = 1.4$ for air. Note that this local temperature increase amounts to an increase in the effective temperature difference felt by the thermal boundary layer. A higher *Nu* is thus not surprising even if other effects are involved.

Next, we look at the influence of the inlet velocity profile. For all cases, a parabolic velocity profile was specified at the inlet. While this is standard practice for incompressible laminar flows, it may not be the most appropriate boundary condition for compressible flows. Computations were performed with a uniform inlet velocity profile. The mass flow rate, *Re*, M_r and other conditions remain the same. However, the maximum velocity and Mach number are lower. The *Nu* and C_f distributions obtained for this case are plotted on Figs. 17 and 18. The maximum values are much lower than those obtained with a parabolic inlet velocity profile. However, away from the symmetry axis the differences are less pronounced. Notice the local maximum on the *Nu* near $r/d = 0.5$, that is close to the radial position of the jet lips. One may conclude that a flat inlet velocity profile is less attractive from an applications's point of view due to its associated lower value of *Nu*.

Finally, we illustrate the ability of the formulation to handle cases where the flow is incompressible in some portion of the domain, anelastic in an other, and compressible in a third one. The equation of state is given by

$$\tilde{\rho} = \frac{\gamma_r M_r^2 \tilde{p} + 1}{(T_s/T_r)\widetilde{T} + 1} \tag{11}$$

In this expression the term $\gamma_r M_r^2 \tilde{p}$ is responsible for compressibility effects (i.e., density changes caused by pressure). The term $(T_s/T_r)\widetilde{T}$ represents thermal expansion effects (i.e., density changes due to temperature variations). One can easily determine and visualize which flow regime occurs in which region of the domain by looking at contours

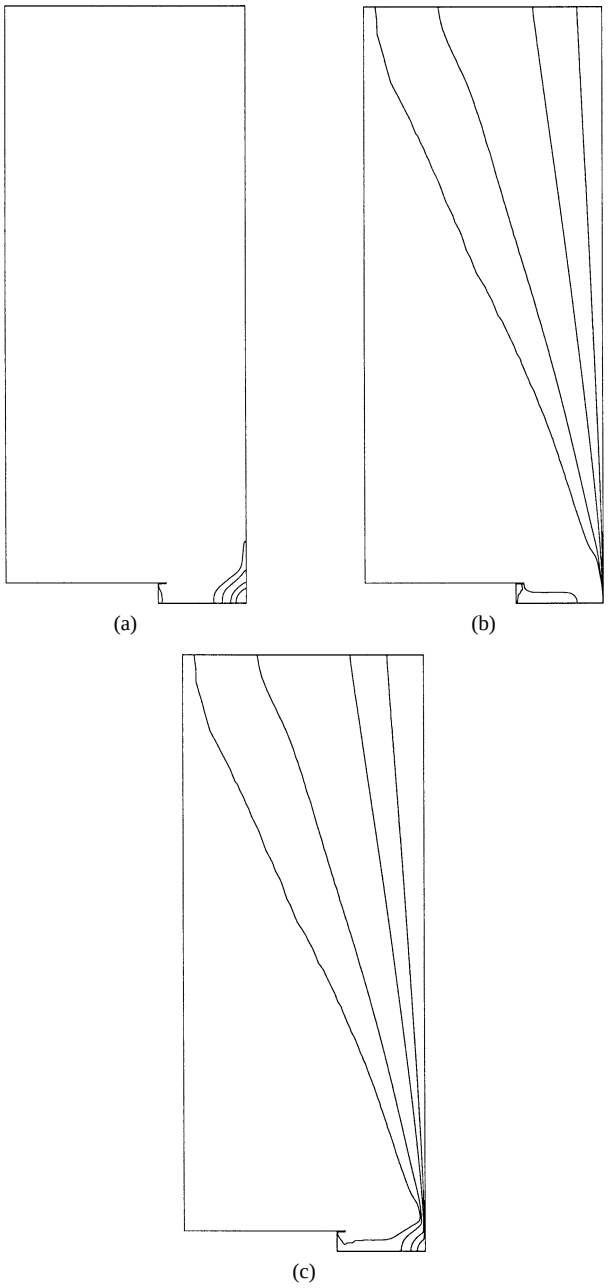

Fig. 22. Density changes due to compressibility and anelastic effects: (a) $\gamma_r M_r^2 \tilde{p}$; (b) $(T_s/T_r)\widetilde{T}$; (c) Density contours.

of $\gamma_r M_r^2 \tilde{p}$ and $(T_s/T_r)\widetilde{T}$. Fig. 22 shows contours of these terms along with contours of density 11 for the air jet at a *Mach* number of 0.5. The areas where the flow is at constant density are clearly visible. Compressibility effects are confined to the vicinity of the stagnation point. Density variations due to temperature are confined to the near wall region. This region is very thin near the stagnation point and thickens with increasing values of the radius. Finally, density contours show clearly where the flow is incompressible and where it is not.

6. Conclusions

A unified formulation of the flow equations was presented to treat three flow regimes: incompressible flow, strongly heated flow, and fully compressible flow. A flow solver using this formulation can handle the simultaneous presence of these regimes in different parts of the domain. Predictions for different flow regimes can be compared with confidence since the discretization is the same for all cases.

An adaptive finite element algorithm using this formulation was applied to compressible laminar impinging round jets with variable fluid properties. Computations on a problem with a closed form solution confirm the good performance of the adaptive methodology. High accuracy is achieved and the error estimates are close to the true error. Applications to jets of air and carbon monoxide also illustrate the high level of accuracy consistently delivered by the methodology. Grid independent solutions are obtained for derived quantities (C_f and *Nu*) even for very thin boundary layers.

Studies on air and CO_2 illustrate the pronounced effect of the temperature dependence of fluid properties on heat transfer and wall shear stress. The effects are more important for CO_2 than for air. Globally, *Nu* and C_f are higher for jets impinging on hot walls, and are lower for cold walls.

Jets at high subsonic Mach number show increases in *Nu* and C_f when compared to strongly heated low Mach number cases. This observation holds for both heated and cooled jets. These increases are largest near the stagnation point. Thus compressibility has a significant impact on the heat transfer characteristics of impinging jets. Finally, a uniform inlet velocity profile generates lower values of *Nu* and C_f than those observed with a parabolic profile.

In summary the unified formulation coupled with adaptivity is a powerful approach to solve complex flow problems. Adaptivity is a simple tool to perform systematic grid refinement studies and to quantify and control the error. Finally, it provides visual cues of solution accuracy and grid convergence.

Acknowledgements

This work was supported in part by NSERC, FCAR, the Canada Research Chair in Multi-disciplinary Analysis and AFOSR grant F49620-96-1-0329.

References

[1] H. Martin, Heat and mass transfer between impinging gas jets and solid surfaces, Adv. Heat Transfer 13 (1977) 1–60.
[2] S.J. Downs, E.H. James, Jet impingement heat transfer—A literature survey, ASME Paper No. 87-HT-35.
[3] S. Polat, B. Huang, A.S. Mujumdar, W.J.M. Douglas, Numerical flow and heat transfer under impinging jets: A review, in: C.L. Tien, T.C. Chawla (Eds.), Annual Review of Numerical Fluid Mechanics and Heat Transfer, Vol. 2, Hemisphere, Washington, DC, 1989, pp. 157–197.

[4] K. Jambunathan, E. Lai, M.A. Moss, B.L. Button, A review of heat transfer data for single circular jet impingement, Internat. J. Heat Fluid Flow 13 (2) (1992) 106–115.
[5] D. Pelletier, F. Ilinca, Adaptive remeshing for the k–ε model of turbulence, AIAA J. 35 (4) (1997) 640–646.
[6] F. Ilinca, D. Pelletier, A. Garon, An adpative finite element method for a two-equation turbulence model in wall-bounded flows, Internat. J. Numer. Methods Fluids 24 (1) (1997) 101–120.
[7] F. Ilinca, D. Pelletier, Positivity preservation and adaptive solution for the k–ε model of turbulence, AIAA J. 36 (1) (1998) 44–50.
[8] D. Pelletier, J.-F. Hétu, F. Ilinca, Adaptive finite element method for thermal flow problems, AIAA J. 32 (4) (1994) 741–747.
[9] D. Pelletier, L. Ignat, F. Ilinca, Adaptive finite element method for conjugate heat transfer, Numer. Heat Transfer, Part A 32 (3) (1997) 267–287.
[10] D. Pelletier, F. Ilinca, É. Turgeon, An adaptive finite element method for forced convection, Internat. J. Numer. Methods Fluids 25 (1997) 803–823.
[11] F. Ilinca, D. Pelletier, A pressure based adaptive finite element algorithm for compressible viscous flows, in: AIAA 34th Aerospace Sciences Meeting and Exhibit, January 15–18, 1996, Reno, NV, AIAA Paper 96-0679.
[12] F. Ilinca, D. Pelletier, A unified approach for adaptive solutions of compressible and incompressible flows, in: AIAA 35th Aerospace Sciences Meeting and Exhibit, January 6–10, 1997, Reno, NV, AIAA Paper 97-0330.
[13] F. Ilinca, D. Pelletier, Adaptive finite element solution of compressible turbulent flows, AIAA J. 36 (12) (1998) 2187–2194.
[14] É. Turgeon, D. Pelletier, Adaptive finite element computation of impinging round jets, in: Proceedings of the Sixth Annual Conference of the Computational Fluid Dynamics Society of Canada, June 7–9, Québec, Canada, 1998, pp. XII.1–XII.6.
[15] É. Turgeon, D. Pelletier, Computation of jet impingement heat transfer by an adaptive finite element algorithm, in: 7th AIAA/ASME Joint Thermophysics and Heat Transfer Conference, June 15–18, 1998, Albuquerque, NM, AIAA Paper 98-2585.
[16] D. Pelletier, F. Ilinca, J.-F. Hétu, Adaptive remeshing for convective heat transer with variable fluid properties, AIAA J. Thermophys. Heat Transfer 8 (4) (1994) 687–694.
[17] T. Aihara, J.K. Kim, S. Maruyama, Effects of temperature-dependent fluid properties on heat transfer due to an axisymmetric impinging gas jet normal to a flat surface, Wärme- und Stoffübertragung 25 (1990) 145–153.
[18] F.S. Sherman, Viscous Flow, McGraw-Hill, New York, 1990.
[19] R.L. Panton, Incompressible Flow, Wiley–Interscience, New York, 1984.
[20] F. Ilinca, D. Pelletier, L. Ignat, Adaptive finite element solution of compressible turbulent flows, in: AIAA 36th Aerospace Sciences Meeting and Exhibit, January 12–15, 1998, Reno, NV, AIAA Paper 98-0229.
[21] J. Peraire, M. Vahdati, K. Morgan, O.C. Zienkiewicz, Adaptive remeshing for compressible flow computations, J. Comput. Phys. 72 (2) (1987).
[22] O.C. Zienkiewicz, J.Z. Zhu, The superconvergent patch recovery and *a posteriori* error estimates. Part 1: The recovery technique, Internat. J. Numer. Methods Engrg. 33 (1992) 1331–1364.
[23] O.C. Zienkiewicz, J.Z. Zhu, The superconvergent patch recovery and *a posteriori* error estimates. Part 2: Error estimates and adaptivity, Internat. J. Numer. Methods Engrg. 33 (1992) 1365–1382.
[24] F. Ilinca, Méthodes d'éléments finis adaptatives pour les écoulements turbulents, Ph.D. Thesis, École Polytechnique de Montréal, 1996.
[25] É. Turgeon, Application d'une méthode d'éléments finis adaptative à des écoulements axisymétriques, Master's Thesis, École Polytechnique de Montréal, 1997.
[26] B. Boroomand, O.C. Zienkiewicz, Recovery by equilibrium in patches (REP), Internat. J. Numer. Methods Engrg. 40 (1997) 137–164.
[27] P.M. Gresho, R.L. Sani, Incompressible Flow and the Finite Element Method, Vol. 2: Isothermal and Laminar Flows, Wiley, New York, 2000.
[28] C.G. Du Toit, Finite element computation of friction factors and Nusselt numbers for rectangular ducts, in: Proceedings of the 2nd Internat. Symp. on Addvances in Computational Heat transfer, Vol. 1, 2001, pp. 583–590.